Evaluation of nano mechanical properties and corrosion behavior of diffusion welded CoCrNi medium-entropy alloy (MEA) and SUS 304 stainless steel joints

Muhammad Samiuddin[a,b,c], Jinglong Li[a b,*], Mudassir Farooq[d], Jiangtao Xiong[a,b,*]

[a] State Key Laboratory of Solidification Processing, Northwestern Polytechnical University, Xi'an, 710072 PR China

[b] Shaanxi Key Laboratory of Friction Welding Technologies, Northwestern Polytechnical University, Xi'an, 710072, PR China

[c] Metallurgical Engineering Department, NED University of Engineering and Technology, Karachi, 75850, Pakistan

[d] Materials Engineering Department, NED University of Engineering and Technology, Karachi, 75850, Pakistan

(*Corresponding author: sami@mail.nwpu.edu.cn; lijinglg@nwpu.edu.cn; xiongjiangtao@nwpu.edu.cn)

ABSTRACT: The study mainly focused on examining nanomechanical properties and corrosion behavior of the weld interface formed by diffusion welding of CoCrNi MEA and SUS 304 stainless steel. Three different bonding temperatures (i.e. 950 °C, 1000 °C, and 1050 °C) were utilized in producing diffusion welded joints. The influence of bonding temperatures on nanomechanical properties of the weld interface was characterized through Nanoindentation tests under various loads (i.e. 20 mN to 100 mN). Additionally, electrochemical properties of the weld interface were also examined using a 0.5 M HCl solution. Results clinched that with the increase of bonding temperature significant suppression in carbide formation occurred along with the weld interface. This instigated a reduction in nano hardness and elastic moduli which resulted in maximum elastic recovery along with the weld interface. The indentation size effect was also evident below 40 mN load after which nano hardness became stable while elastic moduli remained impervious to the change of indentation load. Furthermore, based upon electrochemical properties (i.e. I_{corr}, E_p, and R_p) samples welded at 1000 °C bonding temperature offered excellent corrosion resistance under 0.5M HCl environment.

KEYWORDS: Electrochemical Impedance Spectroscopy (EIS); HCl environment; Medium Entropy Alloy (MEA); Nano-indentation; Potentiodynamic Polarization (PD); SUS 304 Stainless Steel

RESUMEN: *Evaluación de las propiedades nanomecánicas y del comportamiento frente a la corrosión de uniones soldadas por difusión de una aleación de media entropía (MEA) CoCrNi y acero inoxidable SUS 304.* El estudio se centró principalmente en examinar las propiedades nanomecánicas y el comportamiento frente a la corrosión de la interfaz de soldadura formada por el método de soldadura por difusión de de una aleación de media entropía (MEA) CoCrNi y acero inoxidable SUS 304. Se utilizaron tres temperaturas de unión diferentes (950 °C,

1000 °C y 1050 °C) para producir uniones soldadas por difusión. La influencia de las temperaturas de unión en las propiedades nanomecánicas de la interfaz de soldadura se caracterizó mediante ensayos de nanoindentación bajo diversas cargas (de 20 mN a 100 mN). Además, también se examinaron las propiedades electroquímicas de la interfaz de soldadura utilizando una solución de HCl 0,5 M. Los resultados demostraron que con el aumento de la temperatura de unión se producía una supresión significativa de la formación de carburo a lo largo de la interfaz de soldadura. Esto provocó una reducción de la nanodureza y el módulo elástico, lo que dio lugar a una recuperación elástica máxima junto a la interfaz de soldadura. El efecto del tamaño de la indentación también fue evidente por debajo de una carga de 40 mN, después del cual la nanodureza se estabilizó, mientras que los módulos elásticos permanecieron invariables al cambio de la carga de indentación utilizada. Además, basándose en las propiedades electroquímicas (es decir, Icorr, Ep y Rp), las muestras soldadas a una temperatura de unión de 1000 °C ofrecieron una excelente resistencia a la corrosión en un ambiente de HCl 0,5M.

PALABRAS CLAVE: Espectroscopia de Impedancia Electroquímica (EIS); Ambiente HCl; Aleación de Media Entropía (MEA); Nanoindentación; Polarización Potenciodinámica (PD); Acero Inoxidable SUS 304

ORCID ID: Muhammad Samiuddin (https://orcid.org/0000-0002-2350-6114); Jinglong Li (https://orcid.org/0000-0002-3138-2473); Mudassir Farooq (https://orcid.org/0000-0002-5930-4426); Jiangtao Xiong (https://orcid.org/0000-0002-2931-1908)

1. INTRODUCTION

The modern world requires a new alloy that has more flexible mechanical and chemical properties than conventional alloys. The struggle of finding such an alloy system with unique properties that can circumvent conventional alloy had found its baseline after the development of High Entropy alloys (HEAs) also known as Multi Principal Element Alloys (MPEAs). The concept of HEAs was considered the rarely touched alloy in the alloying world until two independent publications in 2004 by Jien-Wei Yeh and Cantor (Cantor *et al.*, 2004; Yeh *et al.*, 2004). These publications brought a new concept of alloy design that began new series of investigations on HEAs. These alloy systems can be classified based on their configuration entropy, if the value of configurational entropy, $\Delta S_{conf} > 1.5R$ (R = universal gas constant), it is considered as High Entropy Alloys; ignoring the fact that whether the HEA is single-phase or multiphase. For MEAs, $1R < \Delta S_{conf} < 1.5R$, and If the value of configurational entropy is less than 1R then it is considered to be Low Entropy Alloys (LEAs) (Yeh, 2013).

Among several MEA systems, CoCrNi is the most common medium entropy alloy with superior mechanical properties unparalleled to any ternary, quaternary, and quinary MEAs to date (Laplanche *et al.*, 2017). The interesting thing to consider was that the tensile strength and ductility of CoCrNi MEAs increased with a decrease in temperature (Gludovatz *et al.*, 2016). Wu *et al.* (2014) studied the CoCrNi MEAs at different compositions and found that all MEAs exhibited high tensile strength and ductility as compared to many HEAs over a wide range of temperatures (-196 °C to 400 °C) (Sathiyamoorthi *et al.*, 2018; Yi *et al.*, 2020; Fang *et al.*, 2021). Adomako *et al.* (2018) investigated the high-temperature oxidation behavior of different MEAs and showed that CoCrNi MEA displayed excellent high-temperature oxidation resistance compared with CoCrNiMn and CoCrNiFeMn MEAs (Adomako *et al.*, 2018). Irradiation resistance of CoCrNi MEA and its corrosion performance under an H_2SO_4 environment were also found satisfactory (Lu *et al.*, 2019; Moravcik *et al.*, 2021). With such extravagant properties, researchers are now compelled to explore the weldability issues associated with CoCrNi MEA. Samiuddin *et al.* (2021), explored the weldability of CoCrNi MEA with SUS 304 stainless steel and concluded that high diffusion bonding temperature embraced defect-free joints which consequently induced maximum shear strength. Du *et al.* (2021) successfully performed diffusion bonding on FGH 98 (Ni-based superalloy) and CoCrNi MEA by utilizing Ni interlayer and achieved maximum shear strength of 592 MPa at 1150 °C (Du *et al.*, 2021). Diffusion bonding on CoCrNi MEA and DD5 (Single crystal Ni-based superalloy) was also executed by Li *et al.* (2021b) The joint received maximum tensile strength (i.e. 1045 MPa) and ductility (22.7%) at high bonding temperature (1110 °C). Sun et al. also successfully performed diffusion bonding between CoCrNi MEA and 316 steel using Spark plasma sintering process and found that with the increase of bonding temperature the tensile strength of the joint exceeded to 80% of 316 stainless steel (Sun *et al.*, 2023). Several authors also performed diffusion bonding to other variants of high entropy alloys and achieved better mechanical properties compared with the other welding processess (Gao *et al.*, 2023; Li *et al.*, 2023).

The microstructure and mechanical performance of the diffusion welded joints can be optimized by characterizing the interface region (bond line), formed between the two metals/alloys. Moreover, the joint quality mainly depends upon interface characteristics which include voids formation, the existence of IMCs, and grain coherency across the interface region. Thus, in this study nanoindentation technique was used to evaluate nano-mechanical properties across the interface. The nanoindentation technique offered a great advantage where tensile or compres-

sion tests are difficult to perform due to sampling size limitations. There are several parameters (i.e. indentation size, indenter geometry, indentation load, holding time, and loading/unloading rate) that can be probed to determine mechanical properties at nano or micro-scale (Ladani *et al.*, 2013; Sadeghilaridjani and Mukherjee, 2020). Recently some research work has been devoted to the nanoindentation of MEAs to establish fundamental knowledge about their deformation mechanisms (Maier-Kiener *et al.*, 2017; Hua *et al.*, 2021). Researchers clinched some interesting features of deformation characteristics of MEAs under nanoindentation such as immobility of dislocations under high entropy effect (Shuang *et al.*, 2021), the influence of severe lattice distortion (Li *et al.*, 2016), and hardness insurgency at low temperature (Alhafez *et al.*, 2021). Although, literature about nanoindentation behavior across the diffusion welded joint is very limited. Only a few studies have been reported so far that utilized nanoindentation to determine the mechanical properties of diffusion welded HEAs (Li *et al.*, 2021a; Peng *et al.*, 2021).

Considering the importance of this novel class of material, researchers also focused on their corrosion behavior. Wang *et al.* (2019) prepared CoCrNi MEA and evaluated its corrosion behavior in both 1 mol/L NaOH and 0.5 mol/L HCl solutions. He found that NiCoCr MEA offered high corrosion resistance than SUS 304 steel in both environments (Wang *et al.*, 2019). An, X, L. et al conducted an electrochemical test on CoNiFe MEA and found that the corrosion rate increased at a higher temperature of NaCl and H_2SO_4 solution (An *et al.*, 2019). Shang, X al investigated the corrosion mechanism of different equiatomic FCC-based entropy alloys i.e., pure Ni, NiCo, NiCoFe, CoCrNi, and CoCrNiFe, and found that Cr element displayed a vital role to enhance the corrosion resistance owing to the formation of stable and compact Cr_2O_3 film. Thus, results concluded that entropy alloys without Cr addition exhibited poor corrosion resistance (Shang *et al.*, 2017). Luo, H et al compared the corrosion response of CoCrFeMnNi HEA with SUS 304 steel in an H_2SO_4 solution and concluded that both the alloys formed passive film. Oxides of Cr, Fe, and Ni mixed with Co and Mn were the main constituents in the passive film of HEA while oxides of Cr and Fe were mainly formed on 304 steel. Moreover, Cr content on the passive film of HEA was well below compared of 304 steel indicating the absence of selective dissolution of the metal element in HEA (Luo *et al.*, 2018). Similarly, Kumar *et al.* (2017), showed that both general and pitting corrosion of Al0.1CoCrFeNi HEA was comparatively better than SUS 304 steel in a 3.5% NaCl solution (Kumar *et al.*, 2017).

Considering the importance of the two alloys, a joint between the two alloys could be used in the equipment such as reactors, heat exchangers, and piping systems CoCrNi weldments are often used in aerospace components such as turbine blades and engine components, while 304 stainless steel is used in structural components. A joint between the two alloys could be used to connect the structural component to the turbine blade or engine component, providing a strong, corrosion-resistant connection (Bridges *et al.*, 2018; Chai and Tassou, 2020; Du *et al.*, 2021). Nowadays, NGNP (next-generation nuclear power plants) commonly employ thin sheet layers with flow channels, bonded using diffusion bonding, to create plate-type or printed circuit heat exchangers (Southall *et al.*, 2008) for 4th generation Nuclear power plants (Clark *et al.*, 2012a; Clark *et al.*, 2012b; Sah *et al.*, 2020). Sine, CoCrNi MEA also possesses excellent corrosion resistance, minimal irradiation damage, and extraordinary fracture toughness with tremendous ductility (Gludovatz *et al.*, 2016; Laplanche *et al.*, 2017; Adomako *et al.*, 2018; Gan *et al.*, 2019; Lu *et al.*, 2019) therefore; the weldment of it can be used to optimize the process.

In the light of the above discussions, it is revealed that no literature is available on the corrosion and nanoindentation behavior of diffusion welded CoCrNi MEA. Therefore, the main objective of this research was to study the nanoindentation behavior across the weld interface of CoCrNi MEA and SUS 304 steel joints and its corrosion response. Three bonding temperatures (i.e. 950 °C, 1000 °C, and 1050 °C) were selected in producing diffusion welded coupons. Nano hardness, elastic moduli, and elastic recovery across the weld interface were determined by the Nanoindentation test against different loads ranging from 20 mN to 100 mN. While the corrosion behavior of the welded coupons was analyzed through potentiodynamic polarization (PD) and electrochemical impedance spectroscopy (EIS) using a 0.5 M HCl environment.

2. MATERIALS AND EXPERIMENTAL PROCEDURE

2.1. Preparation of CoCrNi (MEA)

A vacuum diffusion bonding furnace (FJK-2, China) was used for joining the CoCrNi MEA and SUS 304 alloys. A vacuum arc-melting furnace (VAM) under a high purity argon gas atmosphere with water-cooled copper mold was used to melt and cast the CoCrNi MEA alloy. A batch of 100 g with an equiatomic ratio was placed in the mold such that the element with the highest melting point (Cr) was placed on the top or nearest to the electric arc and the low melting element (Ni) was positioned at the bottom to avoid metal evaporation. The solidified button- ingots were re-melted five times to avoid chemical segregation. To confirm the chemical homogeneity of CoCrNi MEA, elemental mapping was performed using SEM. Figure 1a shows
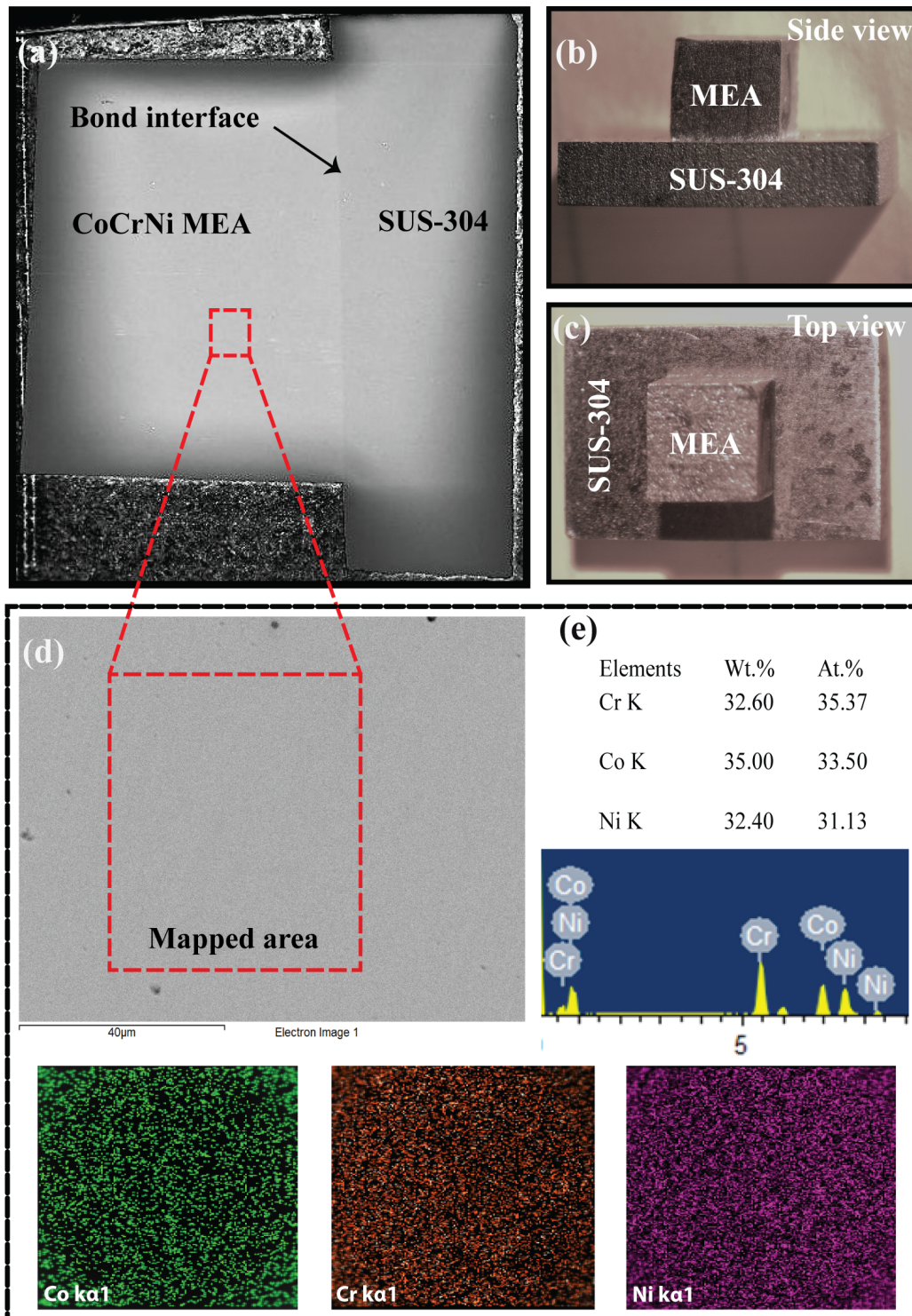
Figure. 1 SEM scans of as prepared CoCrNi MEA (a) location of EDX elemental mapping (b-c) samples macroscopic views, (d) elemental mapping, and (e) composition analysis.

the sample location for elemental mapping and the corresponding SEM scans of as prepared CoCrNi MEA are depicted in Fig. 1(d and e). Macroscopic views of the sample were also presented in Fig. 1(a-c). Results displayed the uniform distribution of all the constituent elements (i.e. Co, Cr, and Ni). Therefore, no evidence for the development of intermetallic compounds was seen which is also consistent with the literature (Wang *et al.*, 2019; Samiuddin *et al.*, 2021; Zhu *et al.*, 2021).

2.2. Diffusion welding of CoCrNi MEA and SUS 304 joints

Before diffusion bonding, the sample's surfaces were grounded and cleaned with acetone for 5 min. After that these samples were assembled in a furnace between the jigs for the bonding process (as shown in Fig. 2a). Samples with faying surfaces parallel to each other were placed in jigs with a thin mica layer between bonded couple material and jig to evade adhesiveness. The alloys were bonded using three different temperatures (i.e. 950 °C, 1000°C, and 1050 °C) at 1 h bonding time and 5 MPa pressure with a vacuum level of 10^{-3} Pa. The welding cycle and other parameters used in the diffusion welding process are shown in Fig. 2b.

2.3. Electrochemical analysis

The corrosion behavior of the diffusion welded samples were studied using a computer-based three-electrode system (Potentiostat G750, Gamry Instruments, USA). The samples were prepared by soldering copper wire at one side followed by epoxy mounting. The samples were ground up to 600 mesh by using silicon carbide paper and polished in alumina suspension. The polished samples were sonicated in ethanol for 30 min to remove surface contamination. The samples were further washed with distilled water and dried with hot air. An area of about 0.3 cm^2 in circular shape was used in such a manner that the bond interface sat along its diameter, enabling a portion of both the alloy exposed to 0.5 M HCl solution. The prepared sample was immediately immersed in the three-electrode electrochemical cell having a one-liter de-aerated solution of 0.5M HCl. The solution was prepared by using 36% pure hydrochloric acid of SigmaAlched® and

the prepared solution was de-aerated by purging argon gas for 30 min from the solution. In the electrochemical cell, the counter electrode was graphite while the reference electrode was Saturated Calomel Electrode (SCE). For electrochemical impedance spectroscopy (EIS) analysis, an open-circuit delay of one hour was given to all samples and the test was conducted in a frequency range of 100 kHz to 0.01 Hz in compliance with ASTM G3-89 and G5-94 standards. For potentiodynamic polarization analysis, the samples were polarized in both cathodic and anodic directions in a potential difference range of ± 0.5 volts vs open-circuit potential. An optical microscope was used to observe the corroded surface after the potentiodynamic polarization test. All the tests were conducted at room temperature in the steady-state conditions and an average of three test results were considered in establishing the results.

2.4. Instrumented nanoindentation tests

Instrumented nanoindentation test was executed on a polished surface of diffusion welded samples using Anton Paar (NHT³, USA) in compliance with ASTM E2546-07 standard. Indenter of Berkovich type (B-U 55) was employed at 50mN/min loading/unloading rate and a holding time of 15 sec was used to eradicate the time-dependent creep response of the specimens. Five different loads ranging from 20 mN to 100 mN (with a 20 mN difference) were applied to determine the nanomechanical properties across the weld interface. After the test, all the specimens were observed using an optical microscope to confirm the correct indenter's position and its impression. Averages of three readings were considered in establishing the results.
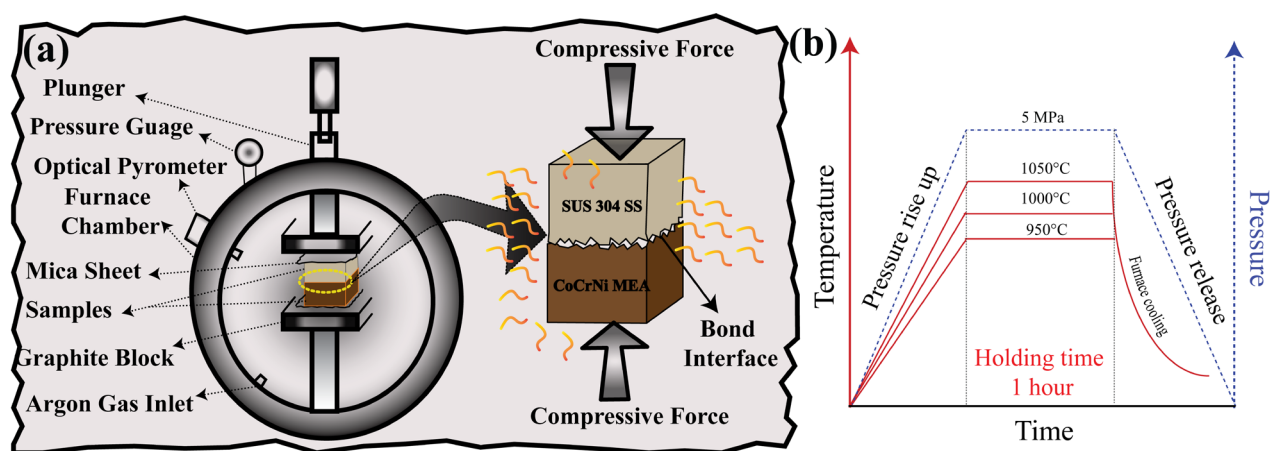
FIGURE 2. Schematic of experimental setup, (a) diffusion welding process, (b) welding cycle used in diffusion bonding of CoCrNi MEA and SUS 304 stainless steel.

3. RESULTS AND DISCUSSION

3.1. Microstructural examination of the weld interface

After metallographic preparation, all the samples were etched through aqua regia (15 ml HCl, 5 ml HNO$_3$) and subsequently, SEM (Tescan Mira 3, The Czech Republic) was used to characterize the weld interface, as depicted in Fig. 3. It can be seen in Fig. 3a that the weld interface formed at 950 °C exhibited the formation of intermetallic compounds (IMCs). Detailed discussion on the nature of these IMCs and their formation can be found in (Muhammad Samiuddin *et al.*, 2021; Samiuddin *et al.*, 2021). In the light of EDX point analysis, it is suggested that most of the IMCs were Cr-rich carbides as shown in Fig 3d. Similar results were also reported in several publications (Muhammad Samiuddin *et al.*, 2021; Samiuddin *et al.*, 2021).

The severity of the formation of such IMCs along with the weld interface drastically reduced at 1000 °C bonding temperature (see Fig 3b). Thus, with the increase of bonding temperature suppression of IMCs formation occurred which is due to the less thermal stability of Cr-rich carbides above 1000 °C (Kleykamp, 2001; Kashaev *et al.*, 2018). Consequently, a negligible amount of IMCs was present along the weld interface formed at 1050 °C bonding temperature, as shown in Fig. 3c. Furthermore, EDX line scanning was utilized to measure the bond interface of the welded joints and representative profiles are displayed in Fig. 3(e and f).

In order to determine the effect of processing parameters on IMCs, its quantitative analysis were also performed using image analysis software. It has been discovered that the size and amount of IMCs decrease over time and with increasing bonding temperature as shown in Table 1. It appeared that the IMCs gradually dissolved during the bonding process, and the rate of dissolution accelerated at higher bonding temperatures. Ultimately, these changes in IMC characteristics have implications on the interface properties. At 950 °C smaller size of IMCs (up to 489 nm) were formed at 1 h bonding time which significantly grew (up to 900 nm) at 3 h bonding time almost double comparative to 1 h bonding time. While at 1000 °C and 1050 °C the IMCs size were further grown with a difference of less than 100 nm within the time span of 1 h to 3 h which indicated that bonding time did not significantly influenced the growth rate of the IMCs. Similar effect of the bonding time was also perceived at 1050 °C at different time span. Although, the area fraction of the IMCs was significantly pretentious with the change of both the parameters. The area fraction of the IMCs was reduced to ~35 % (with 1 h) from ~48 % (with 3 h) at 950 °C, while it further decreased to ~5 % at 1000 °C with 3 h bonding time as depicted in Table 1 and almost shrink to ~0.42% at 1050 °C and 3 h bonding time. This strongly suggested that the IMCs became unstable at higher parametric values and dissolved along the interface due to the paramount effect of IMCs thermodynamics, constituent's atomic diffusion, and their interaction with IMCs, and the concentration gradients across the interface etc.

3.2. Nanoindentation behavior of weld interface

Nano-mechanical properties across the weld interface of diffusion welded samples under different indentation loads were studied using the nanoindentation technique. Parametric loading values were selected in such a way that the corresponding indent size was not exceeded by the width of the weld interface. Thus, loading values of 20 mN to 100 mN were selected which corresponds to less than 9.86 μm maximum indent size. Thereby, the nanoindentation behavior of only weld interfaces under different bonding temperatures was evaluated. A matrix of indents across the weld interface was formed on a well-polished surface of diffusion welded coupons as depicted in Fig. 4. The manner in which indents were taken is shown in Fig. 4d.

A pronounced effect of grain coarsening on the SUS 304 side can be seen on the samples welded at 1050 °C in contrast with other samples (see Figs. 4 (a-c)). However, there were no such appreciable changes in grain size of CoCrNi MEA transpired due to its sluggish diffusion characteristics, attributed to HEAs. Weld interface of 14.25 μm was formed at 1050 °C bonding temperature which was relatively thick compared to 950 °C (9.78 μm) temperature as shown in Fig. 3(e and f). Thus, the thickness of the weld interface was also built up with the increase in welding temperature. Optical images of SUS 304 and CoCrNi MEA are also shown in Fig. 4(e and f) respectively. CoCrNi MEA was etched with acetic glyceregia with the concentration of 15 ml HCL, 10 ml acetic acid, 5 ml HNO3, and 1–2 drops of glycerol, whereas, standard Aqua regia was used for etching SUS 304 stainless steel. It is observed that relatively coarser grains (up to 150 μm) were formed in MEA while SUS 304 stainless steel exhibited a grain size of 25 μm.

Figure 5 depicted load-displacement curves plotted against different nanoindentation loadings using Anton Paar TriTec version 6.0x software. Figure 5a indicated scans of nanoindentation across the weld interface of the 950 °C bonded sample. Significant variations in the slope of the loading curve can be easily grasped. The loading curves became less stepper with the increase of indentation loads which indicated a low deformation rate. Since 950 °C bonded sample contained lots of brittle IMCs along with its
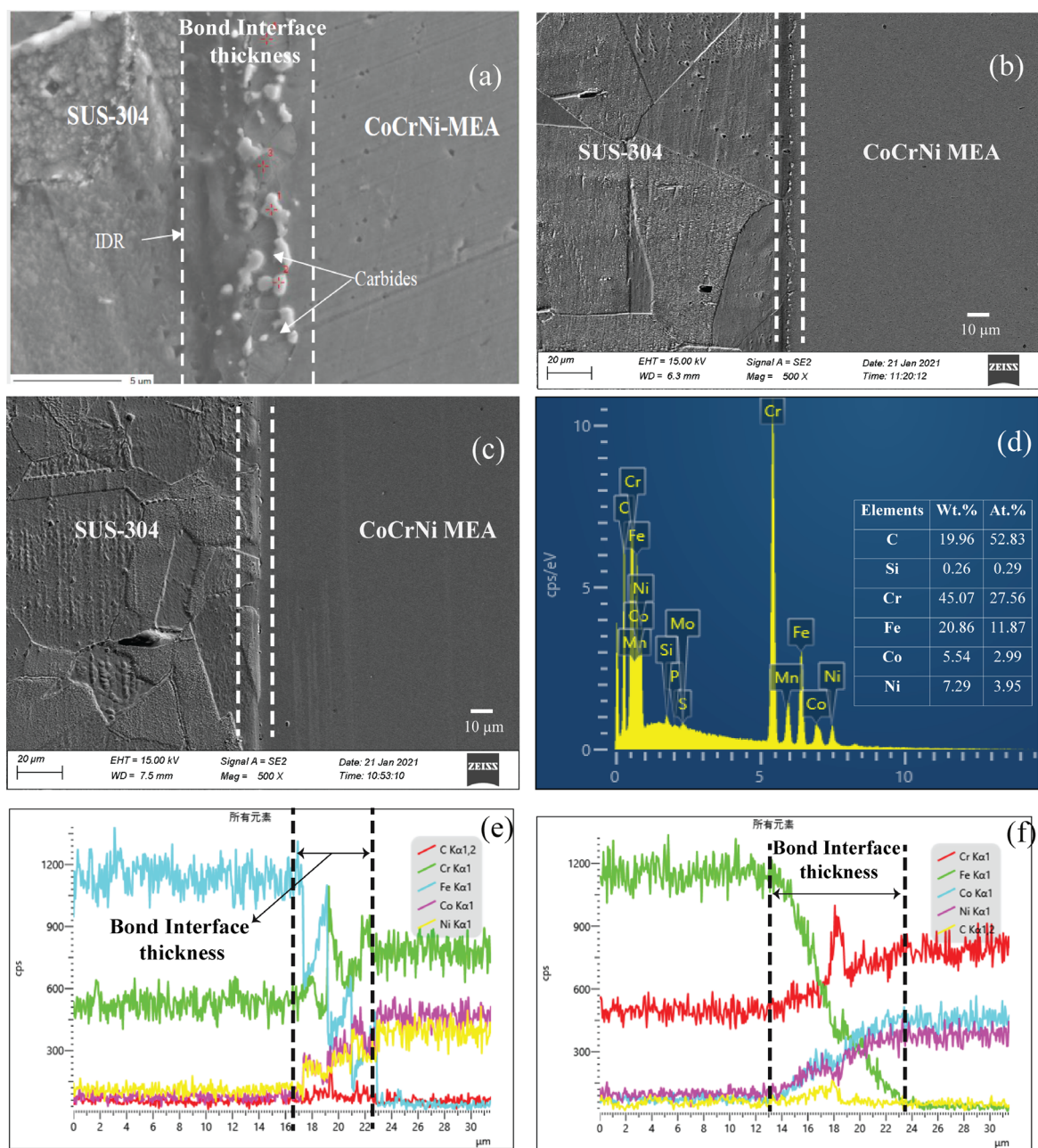
FIGURE 3. SEM scans of diffusion welded samples treated at (a) 950 °C, (b) 1000 °C, (c) 1050 °C bonding temperatures; (d) EDX point analysis of the weld interface marked in a, (e) EDX line profile of the sample welded at 950 °C, and (f) EDX line profile of sample welded at 1050 °C.

TABLE 1. quantitative analysis of the IMCs formed along the bond interface

Temperature (°C)	Size of IMCs (nm)			Area fraction of IMCs (%)		
	At 1 h bonding time	At 2 h bonding time	At 3 h bonding time	At 1 h bonding time	At 2 h bonding time	At 3 h bonding time
950	489	728	900	48	35	41
1000	789	798	849	21	10	5
1050	930	958	999	6	2	0.42
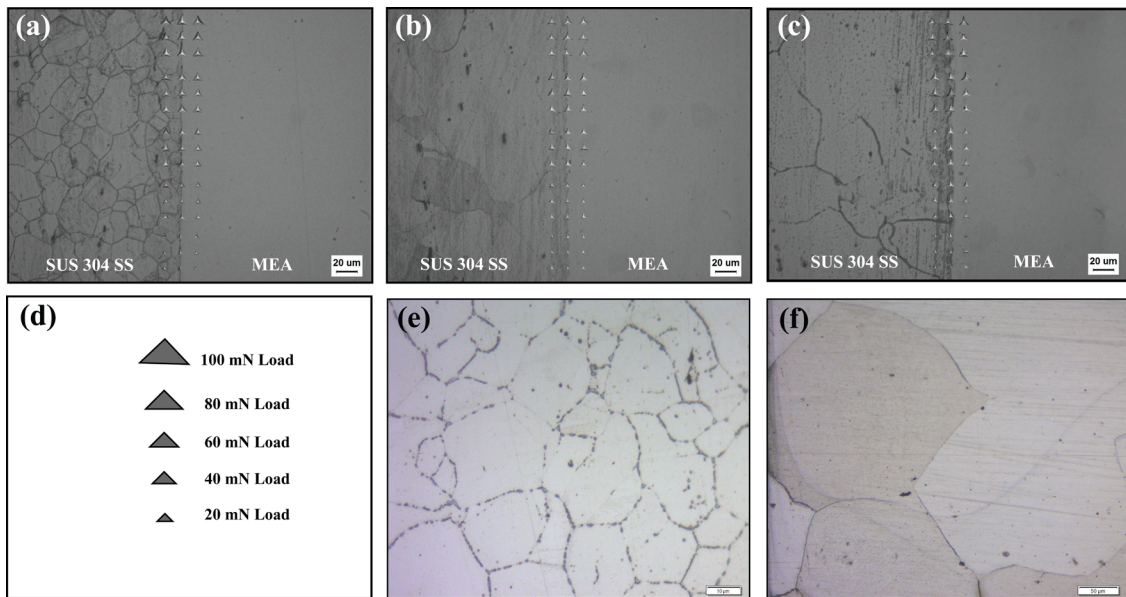
FIGURE 4. Optical images of diffusion welded samples with indent impressions under various loads, joined at (a) 950 °C, (b) 1000 °C, (c) 1050 °C, and (d) schematic of indent's position at corresponding loads, and Optical images of (e) SUS 304 steel, and (f) CoCrNi MEA.
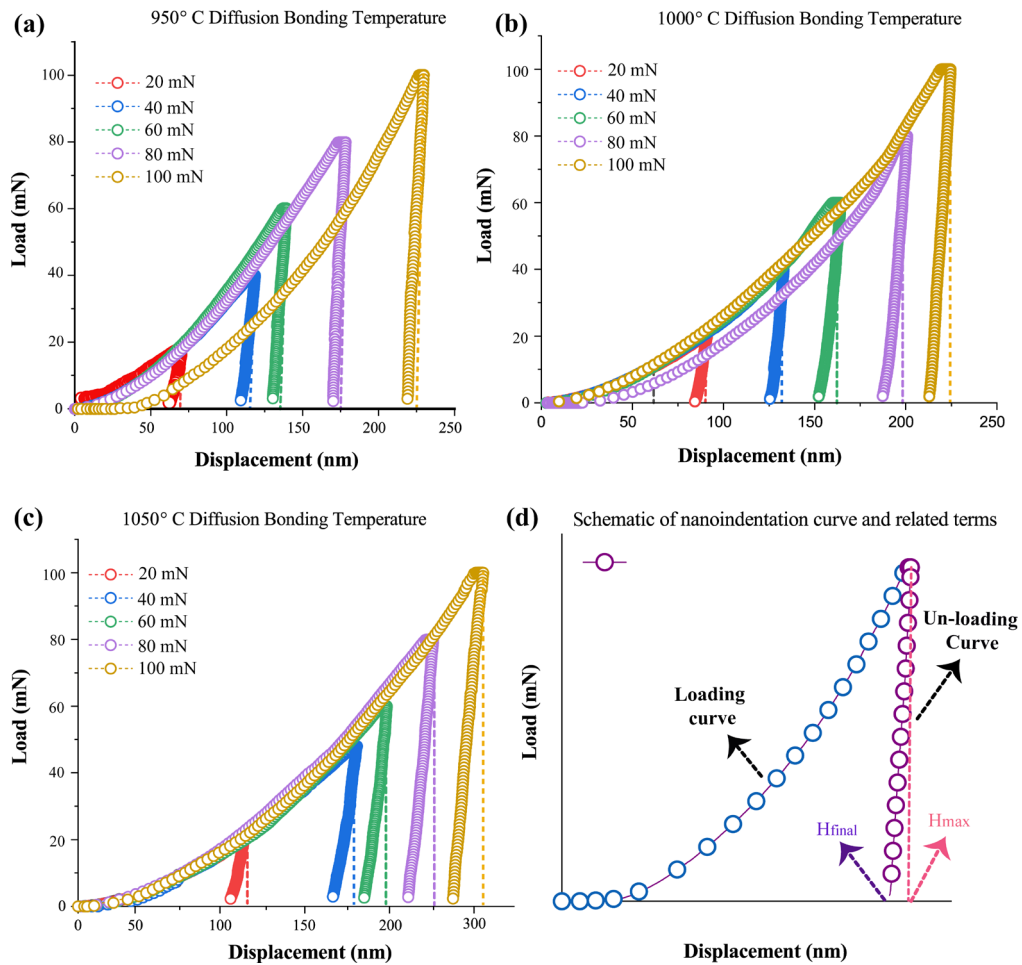
FIGURE 5. Data acquired from instrumented nanoindentation test for diffusion welded samples joined at (a) 950 °C, (b) 1000 °C, (c) 1050 °C, and (d) representation of the terms used in data analysis.

weld interface (see Fig. 3a) which imposed hindrance on deformation. Since at low indentation values the character of IMCs became more prominent due to comparable indent size to IMCs. Similarly, upon increasing indentation load the indent size widened and facilitates deformation due to the combined effect of IMCs and their surrounded region (matrix). The discrepancies in deformation rate upon increasing indentation load became less ascetic on sample welded at 1000 °C bonding temperature as its weld interface contained fewer IMCs compared with 950 °C bonded sample. More IMCs from the weld interface were eradicated with a further increase in welding temperature (i.e. 1050 °C) which subsequently promoted a uniform loading rate on all indentation loads as represented in Fig. 5c.

3.3. Nanomechanical properties of the weld interface

Figure 6 displayed nanomechanical properties extracted from the load-displacement curves (Fig. 5) using the approach proposed by Oliver and Pharr (2004). The nano hardness of SUS 304 steel was found in the range of 4.4 + 2 GPa with an elastic modulus of 225 + 30 GPa under different loads. While CoCrNi MEA exhibited nano hardness and elastic modulus of 3.98 + 1.2 GPa and 290 + 18 GPa respectively. Nano hardness across the weld interface was also mapped by taking the average of three indentations at each load as shown in Fig. 4. Since the nature of weld interface changes with the dissolution of IMCs in response to welding temperature. As a result nanomechanical properties across the weld interface also varied. Figure 6 revealed the variation of nano hardness and elastic moduli as the indentation load and bonding temperature changed. Fig. 6a demonstrates a declining trend of nano hardness with bonding temperature. The maximum value of nano hardness (i.e. 3.82 GPa) was achieved with a sample welded at 950 °C bonding temperature signifying the presence of IMCs. When bonding temperature increases a substantial drop in nano hardness (i.e. 1.58 GPa) was observed associated with carbide dissolution as discussed previously. Another reason that can be attributed to the variation of nano hardness is related to the indentation size effect (ISE).
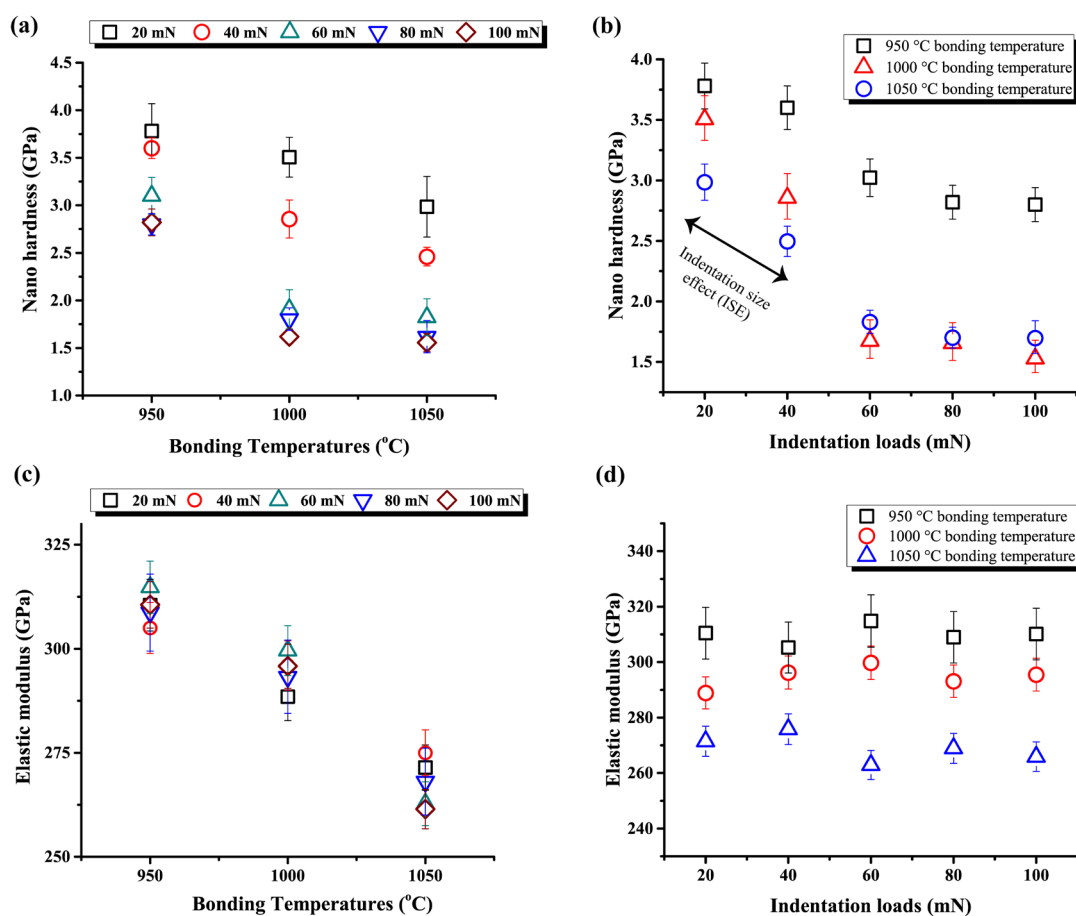
FIGURE 6. Data extracted from nanoindentation test under different loads and bonding temperatures, (a) Nano hardness at different bonding temperatures, (b) Nano hardness under various indentation loads, (c) elastic moduli at different bonding temperatures, and (d) elastic moduli under various indentation loads.

According to the conventional theory of ISE, nano hardness increases with the reduction of indent size due to the dislocation forest hardening mechanism (Voyiadjis and Yaghoobi, 2017). It can be seen that there was a significant increase of nano hardness at low indentation load (i.e. 20 mN) and it progressively drop until at 40 mN load, after which it became stable. This specified that the indentation size effect (ISE) prevailed below 40 mN indentation load also shown in Fig. 6d.

Elastic moduli of all the samples were also calculated from nanoindentation data and the results were plotted in Fig. 6c and d, against various bonding temperatures and indentation loads. Elastic moduli were also influenced by the bonding temperature, a similar decreasing trend in elastic moduli was also observed as in the case with nano hardness. This is due to the presence of IMCs which hindered deformation against the indentation, consequently, both elastic moduli and hardness increase. However, an insignificant change in elastic moduli was observed when different indentation loads were applied as shown in Fig. 6d. This indicated that elastic moduli are insensitive to the change of indentation load.

Figure 7 represented the elastic properties of the weld interface evaluated through a nanoindentation test. It was noticed that indentation depth (H_{final}) increases with the rise of bonding temperature which also reinforced the fact that IMCs became unstable and ultimately dissolved at the high bonding temperature. Thus, with the diminution of IMCs weld interface became more elastic and experienced large deformation. Consequently, higher values of indentation depth (H_{final}) was achieved with increasing indentation load, as depicted in Fig. 7a. Additionally, it was also revealed from Fig. 5 that upon removal of load, strain retrieval transpired from the weld interface resulted in a reduction of H_{final} values with the increase of indentation load. Therefore, elastic recovery offered by the weld interface can be determined from the unloading path by taking the difference between the two indentation depths (i.e. H_{max} & H_{final}) defined in Fig. 5d (Muthupandi *et al.*, 2017). Figure 7b displayed elastic recovery of the weld interface which is also compliant with previous observations. Thus a high yield of elastic recovery is achieved at high bonding temperature due to the elimination of carbides as these carbides offered resistance to deformation (Hussainova *et al.*, 2008). Similarly, the weld interface with lesser IMCs allowed more deformation upon higher indentation load which resulted in higher elastic recovery as shown in Fig. 7b.

In summary, the formation of IMCs influences the deformation rate during the indentation process as indicated in Fig. 5. Changes in the deformation rate can be visually perceived from the variation of slope in the loading curves which was higher in the sample welded at 950 °C as shown in Fig. 5a. Such variation in the slope of loading curves was drastically reduced as the welding temperature increased which might be due to the suppression of IMCs formation (see Fig. 5c). Furthermore, regarding the formation of these brittle IMCs, it was evident from the hardness data that an upshot in Nano hardness was present in the sample welded at 950 °C while it significantly drop with the suppression in IMCs formation as shown in Fig. 6a. However, ISE also prevailed and such effect was impassive when the load was kept higher than 40 mN (see Fig. 6b). Therefore, 60 to 100 mN were the optimized parameter through which the nano-mechanical properties of the welded joints can be determined with certainty. Elastic moduli were also influenced by the presence
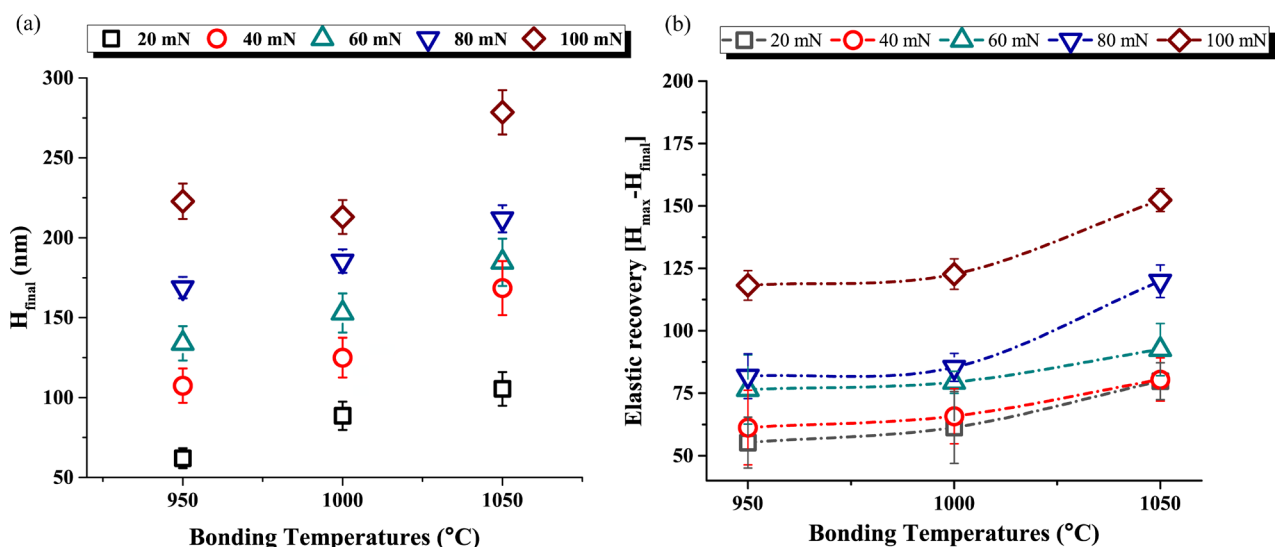
FIGURE 7. Elastic properties of the weld interfaces formed at different bonding temperatures, and against various indentation loads (a) Elastic recoveries versus bonding temperature (b) H_{final} versus bonding temperature.

of such IMCs and it is shown that decreasing trend in the Elastic moduli was observed with the increase in welding temperature (see Fig. 6c). This indicated that the presence of IMCs tends to lower the deformation rate which ultimately increases the Elastic moduli values. Moreover, a significant increase in elastic recovery and h_{final} also represented that these IMCs were brittle, and removal of which induced softness in the weld interface and consequently elastic recovery increases.

3.4. Corrosion behavior of weld interface

This section deals with the corrosion performance of the diffusion welded samples under 0.5M HCl environment. Figure 8 showed the potentiodynamic polarization curves, the pitting potential, and the I_{corr} values of all samples along with their comparison with SUS 304 and CoCrNi MEA. It is observed from Fig. 8a that the E_{corr} value of 304SS (-270 mV) was more negative to CoCrNi alloy (-194 mV) in the given solution. For this reason, SUS 304 acted as an anode when welded with CoCrNi alloy due to the formation of galvanic cells. Also, the corrosion due to galvanic coupling was not much severe as the difference in electrode potential was not significantly high (76 mV) and the coupling was favorable. From Fig. 8b, it is found that E_{corr} of diffusion welded samples were in between the potential value of SUS 304 and CoCrNi MEA. Moreover, the sample diffusion welded at 1000 °C temperature was most electropositive followed by the sample welded at 950 °C and 1050 °C bonding temperature. Figure 8c revealed that the pitting potential of CoCrNi MEA (336 mV) is much higher than SUS 304 (6 mV). After diffusion welding, the pitting potential was significantly dropped as compared to CoCrNi MEA. Among the diffusion welded samples, the sample welded at 1000 °C grasped the highest pitting potential (192 mV) value followed by the sample welded at 950 °C (172 mV),
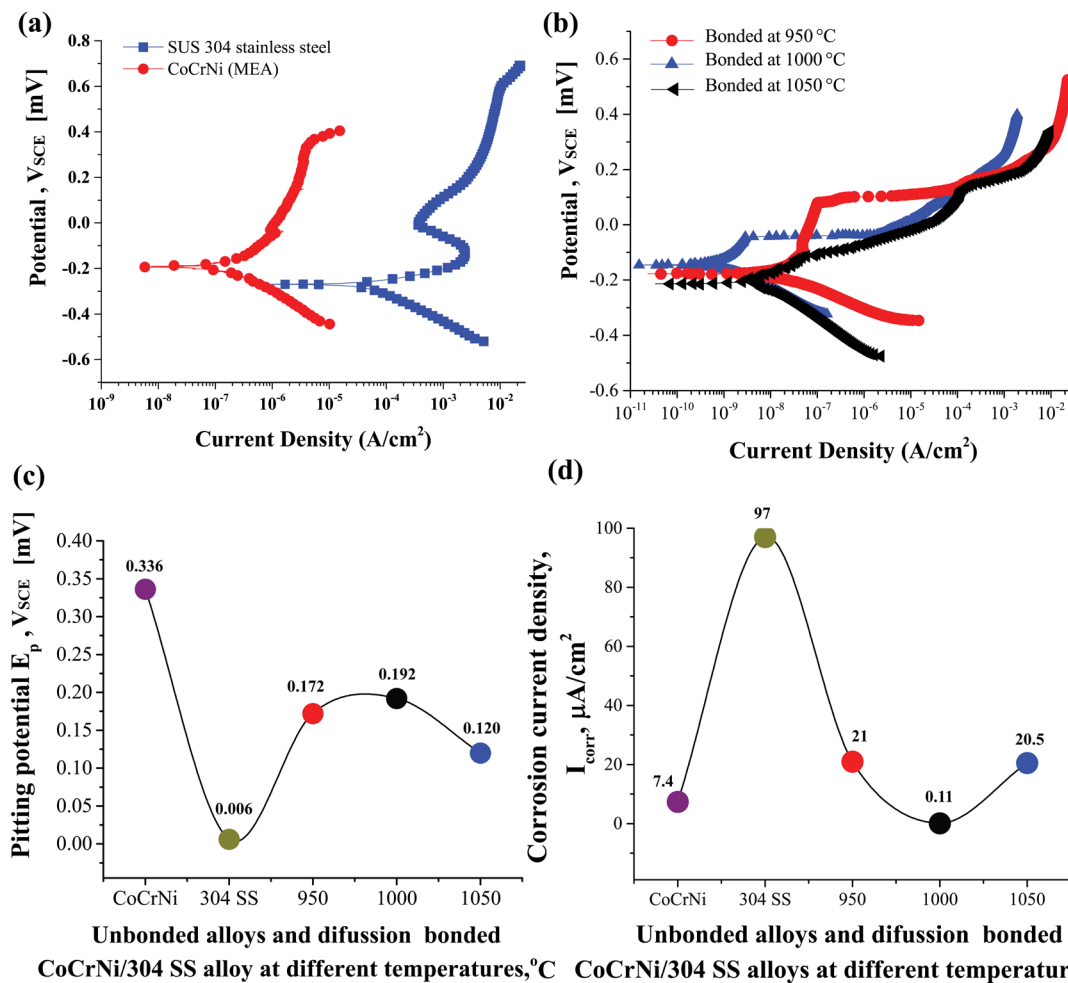
FIGURE 8. Potentiodynamic (PD) scans and electrochemical properties in 0.5M HCl solution. (a) PD curve of 304 stainless steel and CoCrNi medium entropy alloy; (b) PD curve of diffusion welded samples joined at various bonding temperatures; (c) Corrosion current densities "I_{corr}", and (d) Pitting potential "E_p" of SUS 304 SS, CoCrNi MEA, and diffusion welded samples joined at various bonding temperatures.

while the sample welded at 1050 ºC bonding temperature exhibited the lowest pitting potential (120 mV). The corrosion current density (I_{corr}) of all the samples was also calculated from the Tafel analysis and displayed in Fig. 8d. It is found that the I_{corr} value of CoCrNi alloy is much smaller than SUS 304 while among diffusion welded samples, the sample welded at 1000 ºC temperature showed the lowest I_{corr} value; even smaller than CoCrNi MEA. The remaining two diffusion welded samples exhibited the similar I_{corr} value. The corrosion-resistant properties of SUS 304 were found inferior in comparison to CoCrNi alloy because the concentration of corrosion-resistant alloying elements (i.e. Cr, Ni, etc.), was higher in CoCrNi MEA as compared to SUS 304 (Kumar *et al.,* 2017; Luo *et al.*, 2018).

The Nyquist plot, displayed in Fig. 9 compared SUS 304, CoCrNi MEA, and diffusion welded samples at various bonding temperatures. In this plot, the diameter of the half-circle represented the polarization resistance of the samples. This shows that greater the diameter of the half-circle, the higher will be the polarization resistance of the material. Thus, in this regard, the polarization resistance of the sample welded at 1000 ºC is found higher followed by the sample welded at 950 ºC, while the polarization resistance of the sample welded at 1050 ºC was most inferior among all the welded samples. Furthermore, it is also perceived that after diffusion welding polarization resistance increases because the performance of both the alloys before welding was inferior as observed in Fig. 9.
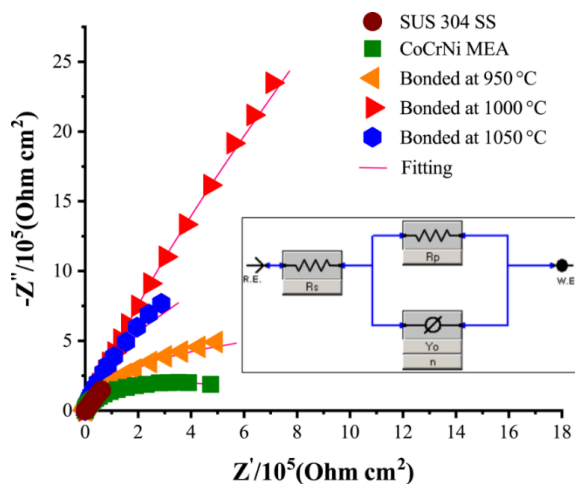
FIGURE 9. Electrochemical impedance spectroscopy (EIS) analysis of welded samples in 0.5M HCl solution.

Table 1 shows the data obtained by fitting Randell modified equivalent circuit as shown in Fig. 9. In this circuit, "Rs" is solution resistance which is attached in series with "Rp"; a polarization resistance and "Yo"; a constant phase element (CPE) magnitude, and

"n" is the CPE exponent. The pure capacitor has been replaced by CPE to minimize the effect of surface irregularities produced during sample preparation and other inherent surface microstructural defects of the material. Double-layer capacitance was calculated by using Eq. (1). Generally, the capacitance has an inverse relation with surface film thickness or in other words, passive layer thickness. The passive layer thickness was calculated by using Eq. (2) and Eq. (3) (Wallinder *et al.,* 1998; Sorour *et al.,* 2021).

$$C_{dl} = Y_o\, \omega_{max}{}^{(n-1)} \qquad (1)$$

$$C = -\left(\omega \times -Z_{img}\right)^{-1} \qquad (2)$$

$$d_{ox} = \frac{\varepsilon}{c} \qquad (3)$$

In equation (1), "ω_{max}" is an angular frequency ($\omega = 2\pi f$) in rad/sec corresponding to the maximum "$-Z_{img}$" value (Machnikova *et al.,* 2008) which was obtained directly from experimental data. Based on "n" value, constant phase element (CPE) can be classified as pure resistance (R) when (n=0), Warburg (W) when (n=0.5) and inductance (L) when (n = -1). CPE was considered as pure double-layer ideal capacitance (C_{dl}) when the value of n = 1 (Behpour *et al.,* 2009). In this case, all samples exhibited both resistive and capacitive behavior. In Eq. (2), "C" is double-layer capacitance, "$-Z_{img}$" and "ω" is an imaginary impedance and angular frequency respectively, corresponding to 1 kHz frequency. In equation (3), "d_{ox}" is passive film thickness, "ε" is the permittivity of the dielectric layer for chromium oxide (Cr_2O_3) which was considered as "12" and "As" is the exposed surface area of the working electrode. Since the sample was immersed in a conductive solution, the permittivity of free space "ε_o" can be omitted (McCafferty, 2010).

From Table 2, it is observed that the polarization resistance of CoCrNi alloy was greater than 304 SUS while the passive film thickness of SUS 304 is slightly greater than CoCrNi MEA. It is also observed that the polarization resistance (R_p) and passive film thickness of diffusion welded samples were greater in comparison to SUS 304 and CoCrNi MEA. Moreover, among diffusion welded samples, it was observed that the polarization resistance and passive film thickness of the sample welded at 1000 ºC were highest as compared with 950 ºC and 1050 ºC. Thus, both R_p and passive film thickness are augmented as bonding temperature increases. From the above discussion, it can be concluded that the optimum bonding temperature concerning polarization resistance and passive film thickness is 1000 ºC.

Surface examination after potentiodynamic scanning was also executed on diffusion welded samples. For this purpose, optical microscopy was utilized and the results are displayed in Fig. 10. It is seen that

TABLE 2. Data extracted from Equivalent circuit from EIS analysis

Parameters	CoCrNi	304SUS	950 ºC	1000 ºC	1050 ºC
R_s, (Ω cm^2)	1.7	1.6	3.3	2.52	1.52
Rp (Ω cm^2)	7.8 x 10^4	5.5 x 10^4	2.5 x 10^6	4.0 x 10^6	40 x 10^4
Yo x10^{-5}	87	4.37	1.97	7.65	4.17
n	0.92	0.74	0.85	0.95	0.74
Cdl (μF cm^{-2})	8.73 x 10^{-4}	2.31 x 10^{-4}	4.31 x 10^{-5}	2.84 x 10^{-5}	7.65 x 10^{-5}
Cdl (μF cm^{-2}) at 1KHz	21.5	4.97	2.7	8.84	4.11
Film Thickness (nm)	6.2	8.0	16.0	49.0	15.0
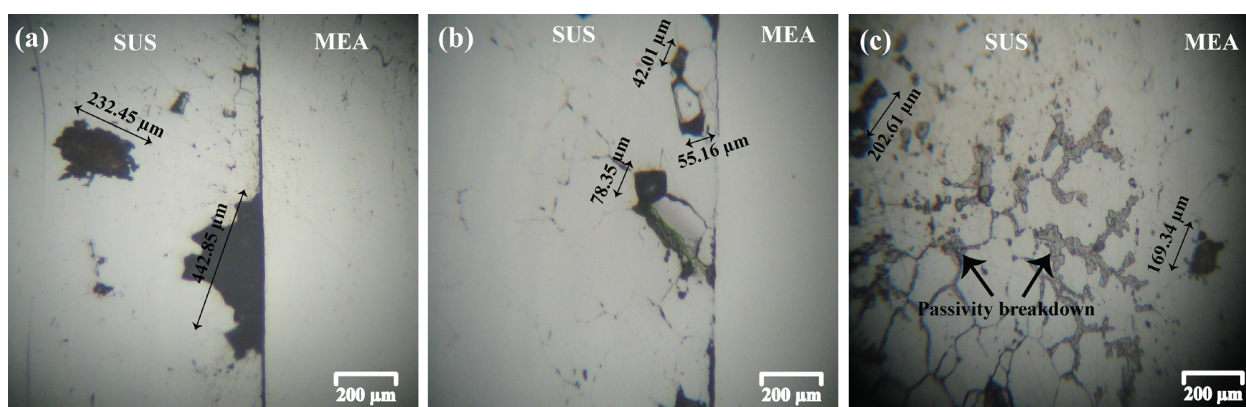
Figure 10. Optical images of diffusion welded samples joined after potentiodynamic polarization test at (a) 950 °C, (b) 1000 °C, (c) 1050 °C, and (d) 1050 °C without polished.

at 950 °C bonding temperature the severity of pit formation was relatively greater. Large patches of materials (pits) up to ~443 μm were removed from SUS 304 steel side while the MEA side remained unaffected which implied that CoCrNi offered excellent resistance against pit formation which is in well agreement with observed results in the potentiodynamic polarization scan. Moreover, corrosion was also anticipated along the weld interface resulting in a thick and prominent dark line as shown in Fig. 10a, with significant removal of material along with the weld interface. As the bonding temperature increased to 1000 °C, the instigation of corrosion shifted towards SUS 304 stainless steel and limited dissolution along the weld interface ensued. Consequently, a significant reduction in pit formation occurred and pit size up to ~78 μm was perceived, as displayed in Fig. 10b. With 1050 °C bonding temperature, the sample contained a pit size up to ~203 μm indicating the corrosion resistance was in between the two welded samples. Moreover, owing to the high bonding temperature, the sample also exhibited intensified intergranular corrosion within SUS 304 side while pit formation ~169 μm was also initiated at the MEA side as shown in Fig. 10c.

Variation in corrosion resistance of diffusion welded samples joined at different bonding temperatures can be explained based upon IMCs formation. Due to the different electrochemical properties of IMCs and the matrix, localized corrosion along the weld interface is instigated in response to the micro galvanic effect between IMCs and the matrix (Silva *et al.*, 2020; Silva *et al.*, 2021). Thus, corrosion resistance increased when the formation of IMCs along the weld interface was inhibited. Although the weld interface at 1050 °C bonding temperature was almost free from IMCs despite this it exhibited poor corrosion resistance. Since at high bonding temperature more Cr is deposited along the grain boundaries (see thick grain boundaries in Fig. 3c, 4c, and 10c) leading to the intergranular corrosion at SUS 304 side. Results obtained from potentiodynamic polarization scanning also supported the observations extracted from optical imaging.

4. CONCLUSION

This work mainly discussed the nanoindentation and corrosion behavior of diffusion welded joints under different processing conditions. The key points of the research findings are as follows:

- Samples of SUS 304 and CoCrNi MEA were joined through a diffusion welding process at different bonding temperatures. IMCs were perceived along with the weld interface and eradicated upon increasing bonding temperature while the thickness of the weld interface widened.
- Nano hardness along the weld interface experienced different values under various indentation loads due to the indentation size effect (ISE) which prevailed up to 40 mN load. Thus, beyond 40 mN load variation in nano hardness became insignificant.
- Nano hardness is greatly affected by bonding temperature, it decreases with the increase of bonding temperature due to suppression of IMCs. Sample welded at 950 °C bonding temperature exhibited the highest value of nano hardness while the lowest amount of elastic recovery was observed due to the presence of IMCs. Moreover, indentation depth (H_{final}) increases with the load and its amplitude further increases with the rise of bonding temperature. Thus, it can be concluded that the weld interface received higher elastic recovery with the reduction of IMCs formation.
- Elastic moduli were also influenced by bonding temperature. At higher bonding temperatures, low values of elastic moduli were observed. However, variation in loadings did not affect elastic moduli, thus almost stable values were achieved under various indentation loads.
- Potentiodynamic scans indicated that the sample welded at 1000 °C exhibited excellent resistance against pit formation, while large size pits were formed at 950 °C and 1050 °C bonding temperature.
- High I_{corr} and low E_{corr} values signified that poor corrosion resistance was offered by 950 °C and 1050 °C bonding temperatures. It is also observed from electrochemical impedance spectroscopy (EIS) that all samples have mixed capacitive and resistive behavior with a single time constant. At 1000 °C bonding temperature, a semi-circle with a large diameter was obtained which represented the highest polarization resistance.
- It was also concluded that the corrosion resistance of diffusion welded samples were greater than pure alloys (i.e. SUS 304 and CoCrNi MEA) and the samples which were diffusion welded at 1000 °C displayed optimum corrosion resistance compared to other diffusion welded samples.

REFERENCES

Adomako, N.K., Kim, J.H., Hyun, Y.T. (2018). High-temperature oxidation behaviour of low-entropy alloy to medium- and high-entropy alloys. *J. Therm. Anal. Calorim.* 133 (1), 13-26. https://doi.org/10.1007/s10973-018-6963-y.

Alhafez, I.A., Ruestes, C.J., Zhao, S., Minor, A.M., Urbassek, H.M. (2021). Dislocation structures below a nano-indent of the CoCrNi medium-entropy alloy. *Mater. Lett.* 283, 128821. https://doi.org/10.1016/j.matlet.2020.128821.

An, X.L., Zhao, H., Chu, C.L., Dai, T., Lu, T., Huang, Z.H., Guo, C., Chu, P.K. (2019). Hall-Petch relationship and corrosion behavior of cold-rolled CoNiFe medium entropy alloy. *J. Alloys Compd.* 807, 151698. https://doi.org/10.1016/j.jallcom.2019.151698.

Behpour, M., Ghoreishi, S.M., Soltani, N., Salavati-Niasari, M. (2009). The inhibitive effect of some bis-N, S-bidentate Schiff bases on corrosion behaviour of 304 stainless steel in hydrochloric acid solution. *Corros. Sci.* 51 (5), 1073-1082. https://doi.org/10.1016/j.corsci.2009.02.011.

Bridges, D., Zhang, S., Lang, S., Gao, M., Yu, Z., Feng, Z., Hu, A. (2018). Laser brazing of a nickel-based superalloy using a Ni-Mn-Fe-Co-Cu high entropy alloy filler metal. *Mater. Letters* 215, 11-14. https://doi.org/10.1016/j.matlet.2017.12.003.

Cantor, B., Chang, I.T., Knight, P., Vincent, A.J. (2004). Microstructural development in equiatomic multicomponent alloys. *Mater. Sci. Eng. A* 375-377, 213-218. https://doi.org/10.1016/j.msea.2003.10.257.

Chai, L., Tassou, S.A. (2020). A review of printed circuit heat exchangers for helium and supercritical CO_2 Brayton cycles. *Therm. Sci. Eng. Prog.* 18, 100143. https://doi.org/10.1016/j.tsep.2020.100543.

Clark, D.E., Mizia, R.E., Piyush, S. (2012a). Diffusion Welding of Alloys for Molten Salt Service – Status Report. USA, pp. 1-19. https://www.osti.gov/biblio/1070108.

Clark, D.E., Mizia, R.E., Glazoff, M.V., Patterson, M.W. (2012b). Diffusion Welding of Compact Heat Exchangers for Nuclear Applications. Idaho National Laboratory, Idaho Falls, Idaho, USA, pp. 1-28.

Du, Y., Li, Z., Xiong, J., Chen, Y., Li, S., Li, J., Dong, J. (2021). Diffusion Bonding of FGH 98 and CoCrNi-Based Medium-Entropy Alloy: Microstructure Evolution and Mechanical Tests. *Crystals* 11 (10), 1158. https://doi.org/10.3390/cryst11101158.

Fang, J.Y.C., Liu, W.H., Luan, J.H., Jiao, Z.B. (2021). Phase Stability and Precipitation in L12-Strengthened CoCrNi Medium-Entropy Alloys at Intermediate Temperatures. *J. Phase Equilib. Diffus.* 42 (5), 781-793. https://doi.org/10.1007/s11669-021-00919-4.

Gan, B., Wheeler, J.M., Bi, Z., Liu, L., Zhang, J., Fu, H. (2019). Superb cryogenic strength of equiatomic CrCoNi derived from gradient hierarchical microstructure. *J. Mater. Sci. Technol.* 35 (6), 957-961. https://doi.org/10.1016/j.jmst.2018.12.002.

Gao, H., He, G., Li, Q., Li, Y., Hu, W., Zhou, S., Liu, F., Yi, J., Zhang, Y., Cai, Z., Ogata, S., Qiao, L., Gao, L. (2023). Diffusion bonding of high entropy alloy and stainless steel at a relative lower temperature via surface nano-crystallization treatment. *J. Mater. Res. Technol.* 24, 475-487. https://doi.org/10.1016/j.jmrt.2023.03.026.

Gludovatz, B., Hohenwarter, A., Thurston, K.V., Bei, H., Wu, Z., George, E.P., Ritchie, R.O. (2016). Exceptional damage-tolerance of a medium-entropy alloy CrCoNi at cryogenic temperatures. *Nat. Commun.* 7 (1), 10602. https://doi.org/10.1038/ncomms10602.

Hua, D., Xia, Q., Wang, W., Zhou, Q., Li, S., Qian, D., Shi, J., Wang, H. (2021). Atomistic insights into the deformation mechanism of a CoCrNi medium entropy alloy under nanoindentation. *Int. J. Plas.* 142, 102997. https://doi.org/10.1016/j.ijplas.2021.102997.

Hussainova, I., Jasiuk, I., Du, X., Cabassa, D. Pirso, J. (2008). *Mechanical properties of chromium carbide based cermets at micro - level*. In *Advances in powder metallurgy & particulate materials*. PowderMet 2008, Washington, DC, USA.

Kashaev, N., Ventzke, V., Stepanov, N., Shaysultanov, D., Sanin, V., Zherebtsov, S. (2018). Laser beam welding of a CoCrFeNiMn-type high entropy alloy produced by self-propagating high-temperature synthesis. *Intermetallics* 96, 63-71. https://doi.org/10.1016/j.intermet.2018.02.014.

Kleykamp, H. (2001). Thermodynamic studies on chromium carbides by the electromotive force (emf) method. *J. Alloys Compd.* 321 (1), 138-145. https://doi.org/10.1016/S0925-8388(01)01012-X.

Kumar, N., Fusco, M., Komarasamy, M., Mishra, R.S., Bourham, M., Murty, K.L. (2017). Understanding effect of 3.5 wt.% NaCl on the corrosion of Al0.1CoCrFeNi high-entropy alloy. *J. Nucl. Mater.* 495, 154-163. https://doi.org/10.1016/j.jnucmat.2017.08.015.

Ladani, L., Harvey, E., Choudhury, S.F., Taylor, C.R. (2013). Effect of Varying Test Parameters on Elastic–plastic Properties Extracted by Nanoindentation Tests. *Exp. Mech.* 53 (8), 1299-1309. https://doi.org/10.1007/s11340-013-9732-7.

Laplanche, G., Kostka, A., Reinhart, C., Hunfeld, J., Eggeler, G., George, E.P. (2017). Reasons for the superior mechanical properties of medium-entropy CrCoNi compared to high-entropy CrMnFeCoNi. *Acta Mater.* 128, 292-303. https://doi.org/10.1016/j.actamat.2017.02.036.

Li, J., Fang, Q., Liu, B., Liu, Y.W., Liu, Y. (2016). Atomic-scale analysis of nanoindentation behavior of high-entropy alloy. *J. Micromech. Mol. Phys.* 1 (1), 1650001. https://doi.org/10.1142/S2424913016500016.

Li, S., Li, J., Shi, J., Du, Y., Peng, Y., Jin, F., Xiong, J., Zhang, F. (2021a). Microstructure and mechanical properties of the brazed region in the AlCoCrFeNi high-entropy alloy and FGH98 superalloy joint. *Mater. Sci. Eng. A* 804, 140714. https://doi.org/10.1016/j.msea.2020.140714.

Li, S., Sun, X., Du, Y., Peng, Y., Chen, Y., Li, Z., Xiong, J., Li, J. (2021b). Microstructure and Mechanical Properties of Diffusion-Bonded CoCrNi-Based Medium-Entropy Alloy to DD5 Single-Crystal Superalloy Joint. *Crystals* 11 (9), 1127. https://doi.org/10.3390/cryst11091127.

Li, P., Sun, H.-t., Li, C., Wu, B.-s., Yang, J., Jiang, Y., Dong, H.-g (2023). A novel strengthening strategy for diffusion bonded joint of AlCoCrFeNi2.1 eutectic high entropy alloy to 304 stainless steel. *Trans. Nonferrous Met. Soc. China* 33 (7), 2121-2135. https://doi.org/10.1016/S1003-6326(23)66248-X.

Lu, C., Yang, T.-N., Jin, K., Velisa, G., Xiu, P., Peng, Q., Gao, F., Zhang, Y., Bei, H., Weber, W.J., Wang, L. (2019). Irradiation effects of medium-entropy alloy NiCoCr with and without pre-indentation. *J. Nucl. Mater.* 524, 60-66. https://doi.org/10.1016/j.jnucmat.2019.06.020.

Luo, H., Li, Z., Mingers, A.M., Raabe, D. (2018). Corrosion behavior of an equiatomic CoCrFeMnNi high-entropy alloy compared with 304 stainless steel in sulfuric acid solution. *Corros. Sci.* 134, 131-139. https://doi.org/10.1016/j.corsci.2018.02.031.

Machnikova, E., Whitmire, K.H., Hackerman, N. (2008). Corrosion inhibition of carbon steel in hydrochloric acid by furan derivatives. *Electrochim. Acta* 53 (20), 6024-6032. https://doi.org/10.1016/j.electacta.2008.03.021.

Maier-Kiener, V., Schuh, B., George, E.P., Clemens, H., Hohenwarter, A. (2017). Nanoindentation testing as a powerful screening tool for assessing phase stability of nanocrystalline high-entropy alloys. *Mater. Des.* 115, 479-485. https://doi.org/10.1016/j.matdes.2016.11.055.

McCafferty, E. (2010). *Introduction to corrosion science*. Springer Science & Business Media.

Moravcik, I., Peighambardoust, N.S., Motallebzadeh, A., Moravcikova-Gouvea, L., Liu, C., Prabhakar, J.M., Dlouhy, I., Li, Z. (2021). Interstitial nitrogen enhances corrosion resistance of an equiatomic CoCrNi medium-entropy alloy in sulfuric acid solution. *Materials Characterization* 172, 110869. https://doi.org/10.1016/j.matchar.2020.110869.

Muhammad Samiuddin., Jinglong, L., Siddiqui, M.A., Jiangtao, X., Ling, R. (2021). Electrochemical Corrosion Behavior of CoCrNi Medium Entropy Alloy and SUS-304 Stainless Steel Diffusion Welded Joints at Various Bonding Temperatures. *Phys. Metals Metallogr.* 122 (14), 1561-1571. https://doi.org/10.1134/S0031918X21140234.

Muthupandi, G., Lim, K.R., Na, Y.-S., Park, J., Lee, D., Kim, H., Park, S., Choi, Y.S. (2017). Pile-up and sink-in nanoindentation behaviors in AlCoCrFeNi multi-phase high entropy alloy. *Mater. Sci. Eng. A* 696, 146-154. https://doi.org/10.1016/j.msea.2017.04.045.

Oliver, W.C., Pharr, G.M. (2004). Measurement of hardness and elastic modulus by instrumented indentation: Advances in understanding and refinements to methodology. *J. Mater. Res.* 19 (1), 3-20. https://doi.org/10.1557/jmr.2004.19.1.3.

Peng, Y., Li, J., Shi, J., Li, S., Xiong, J. (2021). Microstructure and mechanical properties of diffusion bonded joints of high-entropy alloy Al5(HfNbTiZr)95 and TC4 titanium alloy. *J. Mater. Res. Technol.* 11, 1741-1752. https://doi.org/10.1016/j.jmrt.2021.02.003.

Sadeghilaridjani, M., Mukherjee, S. (2020). High-Temperature Nano-Indentation Creep Behavior of Multi-Principal Element Alloys under Static and Dynamic Loads. *Metals* 10 (2), 250. https://doi.org/10.3390/met10020250.

Sah, I., Hwang, J.-B., Kim, W.-G., Kim, E.-S., Kim, M.-H. (2020). High-temperature mechanical behaviors of diffusion-welded Alloy 617. *Nuclear Engineering and Design* 364, 1106-1121.

Samiuddin, M., Li, J., Chandio, A.D., Muzamil, M., Siddiqui, S.U., Xiong, J. (2021). Diffusion welding of CoCrNi medium entropy alloy (MEA) and SUS 304 stainless steel at different bonding temperatures. *Weld. World* 65 (11), 2193-2206. https://doi.org/10.1007/s40194-021-01165-5.

Sathiyamoorthi, P., Bae, J.W., Asghari-Rad, P., Park, J.M., Kim, J.G., Kim, H.S. (2018). Effect of Annealing on Microstructure and Tensile Behavior of CoCrNi Medium Entropy Alloy Processed by High-Pressure Torsion. *Entropy* 20 (11), 849. https://doi.org/10.3390/e20110849.

Shang, X., Wang, Z., He, F., Wang, J., Li, J., Yu, J.K. (2017). The intrinsic mechanism of corrosion resistance for FCC high entropy alloys. *Sci. China Technol. Sci.* 61 (2), 189-196. https://doi.org/10.1007/s11431-017-9114-1.

Shuang, S., Lu, S., Zhang, B., Bao, C., Kan, Q., Kang, G., Zhang, X. (2021). Effects of high entropy and twin boundary on the nanoindentation of CoCrNiFeMn high-entropy alloy: A molecular dynamics study. *Comput. Mater. Sci.* 195, 110495. https://doi.org/10.1016/j.commatsci.2021.110495.

Silva, D.D.S., Lima, L., Araujo, A.J.M., Silva, V.D., Raimundo, R.A., Damasceno, I. Z., Simoes, T.A., Gomes, R.M. (2020). The Effect of Microstructural Changes on Mechanical and Electrochemical Corrosion Properties of Duplex Stainless Steel Aged for Short Periods. *Materials* 13 (23), 5511. https://doi.org/10.3390/ma13235511.

Silva, D.D.S., Simões, T.A., Macedo, D.A., Bueno, A.H.S., Torres, S.M., Gomes, R.M. (2021). Microstructural influence of sigma phase on pitting corrosion behavior of duplex stainless steel/NaCl electrolyte couple. *Mater. Chem. Phys.* 259, 124056. https://doi.org/10.1016/j.matchemphys.2020.124056.

Sorour, A.A., Farooq, M., Mekki, A., Kumar, A.M. (2021). Corrosion of a Spark Plasma Sintered Fe-Cr-Mo-BC Alloy in Hydrochloric Acid. *Metallogr. Microstruct. Anal.* 10 (3), 291-301. https://doi.org/10.1007/s13632-021-00739-5.

Southall, D., Pierres, R. Le, Dewson, S.J. (2008). Design considerations for compact heat exchangers. United States, American Nuclear Society - ANS.

Sun, H., Hashimoto, N., Oka, H. (2023). Vacuum diffusion bonding between equiatomic CoCrNi-based concentrated solid solution alloys system and 316 stainless steel by spark plasma sintering. *Mater. Sci. Eng. A* 879, 145297. https://doi.org/10.1016/j.msea.2023.145297.

Voyiadjis, G.Z., Yaghoobi, M. (2017). Review of Nanoindentation Size Effect: Experiments and Atomistic Simulation. *Crystals* 7 (10), 321. https://doi.org/10.3390/cryst7100321.

Wallinder, D., Pan, J., Leygraf, C., Delblanc-Bauer, A. (1998). EIS and XPS study of surface modification of 316LVM stainless steel after passivation. *Corros. Sci.* 41 (2), 275-289. https://doi.org/10.1016/S0010-938X(98)00122-X.

Wang, J., Yang, H., Ruan, J., Wang, Y., Ji, S. (2019). Microstructure and properties of CoCrNi medium-entropy alloy produced by gas atomization and spark plasma sintering. *J. Mater. Res.* 34 (12), 2126-2136. https://doi.org/10.1557/jmr.2019.96.

Wu, Z., Bei, H., Otto, F., Pharr, G.M., George, E.P. (2014). Recovery, recrystallization, grain growth and phase stability of a family of FCC-structured multi-component equiatomic solid solution alloys. *Intermetallics* 46, 131-140. https://doi.org/10.1016/j.intermet.2013.10.024.

Yeh, J.W., Chen, S.K., Lin, S.J., Gan, J.I., Chin, T.S., Shun, T.T., Tsau, C.H., Chang, S.Y. (2004). Nanostructured high-entropy alloys with multiple principal elements: novel alloy design concepts and outcomes. *Adv. Eng. Mater.* 6 (5), 299-303. https://doi.org/10.1002/adem.200300567.

Yeh, J.-W. (2013). Alloy design strategies and future trends in high-entropy alloys. *JOM* 65 (12), 1759-1771. https://doi.org/10.1007/s11837-013-0761-6.

Yi, H., Bi, M., Yang, K., Zhang, B. (2020). Significant Improvement the Mechanical Properties of CoCrNi Alloy by Tailoring a Dual FCC-Phase Structure. *Materials* 13 (21), 4909. https://doi.org/10.3390/ma13214909.

Zhu, M., He, F., Yuan, Y., Guo, S., Wei, G. (2021). A comparative study on the corrosion behavior of CoCrNi medium-entropy alloy and 316L stainless steel in simulated marine environment. *Intermetallics* 139, 107370. https://doi.org/10.1016/j.intermet.2021.107370.